

The CLAS12 beamline and its performance

N. Baltzell^a, V. Burkert^a, J. Carvajal^f, N. Dashyan^b, R. De Vita^c, L. Elouadrhiri^a, G. Kharashvili^a, A. Kim^d, R. Paremuzyan^e, B. A. Raue^f, S. Stepanyan^a, M. Ungaro^a, K. Wild^f

^aThomas Jefferson National Accelerator Facility, Newport News, Virginia 23606

^bAlikhanian National Laboratory, Yerevan, Armenia

^cIstituto Nazionale di Fisica Nucleare, Genova, Via Dodecaneso 33, 16146 Italy

^dUniversity of Connecticut, Storrs, CT 06269-3046

^eUniversity of New Hampshire, Department of Physics, Durham, NH 03824

^fFlorida International University, Miami, FL 33199

Abstract

This paper describes the Hall B beamline and its performance during the first year of data-taking operation using the CLAS12 detector. We review the beamline instrumentation used to measure and monitor the beam. This instrumentation led to excellent beam quality for energies ranging from 2.3 to 10.6 GeV at the design luminosity of $10^{35} \text{ cm}^{-2}\text{s}^{-1}$. The instrumentation includes a Møller polarimeter, which can typically measure the beam polarization to an absolute precision of $\sim 2.5\%$.

Keywords: electron beam, collimator, heavy photon, electromagnetic calorimeter, polarimeter

1. Introduction

The physics program for CLAS12 in Jefferson Lab's Hall B requires the use of electron beams of various energies and currents that impinge upon on targets ranging from liquid hydrogen to lead. A significant part of the physics program includes running with polarized targets that require a rastered beam on the target. In order to extract experimental observables, accurate measurements of the beam charge and polarization are required. Also, for safe and efficient operation of a large, open acceptance spectrometer, proper shielding and a stable beam with a small lateral size and minimal beam halo are needed.

The Hall-B beamline is designed to satisfy experimental requirements and provide necessary controls and monitoring of the electron beam properties for safe and efficient operation of CLAS12. The key set of parameters required by experiments with CLAS12 is listed in Table 1. The main challenges for the beamline setup are the open acceptance of CLAS12 and the close proximity of various sensitive detectors to the target and beam. Such challenges were successfully overcome in Hall B in the past for CLAS [1] experiments and the Heavy Photon Search (HPS) experiment [2].

A few key modifications to the beamline [3] used during the lower-energy run of the HPS experiment

Parameter	Requirement	Unit
E	≤ 11	GeV
$\delta p/p$	$< 10^{-4}$	
Current	50 to 500	nA
Current instability	~ 10	%
σ_x, σ_y	< 300	μm
Position stability	< 200	μm
Divergence	< 100	μrad
Beam halo ($> 5\sigma$)	$< 10^{-4}$	
Beam polarization	> 0.85	

Table 1: Nominal required Hall B beam parameters.

have been introduced in order to establish high-quality physics beams in Hall B and run CLAS12 at the design luminosity of $10^{35} \text{ cm}^{-2}\text{s}^{-1}$. Additions to the beamline for high-energy running of CLAS12 include a new intermediate beam dump upstream of the hall, a cryogenic target system, shielding downstream of the target to protect CLAS12 detectors from electromagnetic backgrounds, and the Møller polarimeter for beam polarization measurements.

This paper will discuss the design of the Hall-B beamline for CLAS12, and its performance during the 2018 experimental run. It will review the beamline instrumentation used to measure and monitor beam pa-

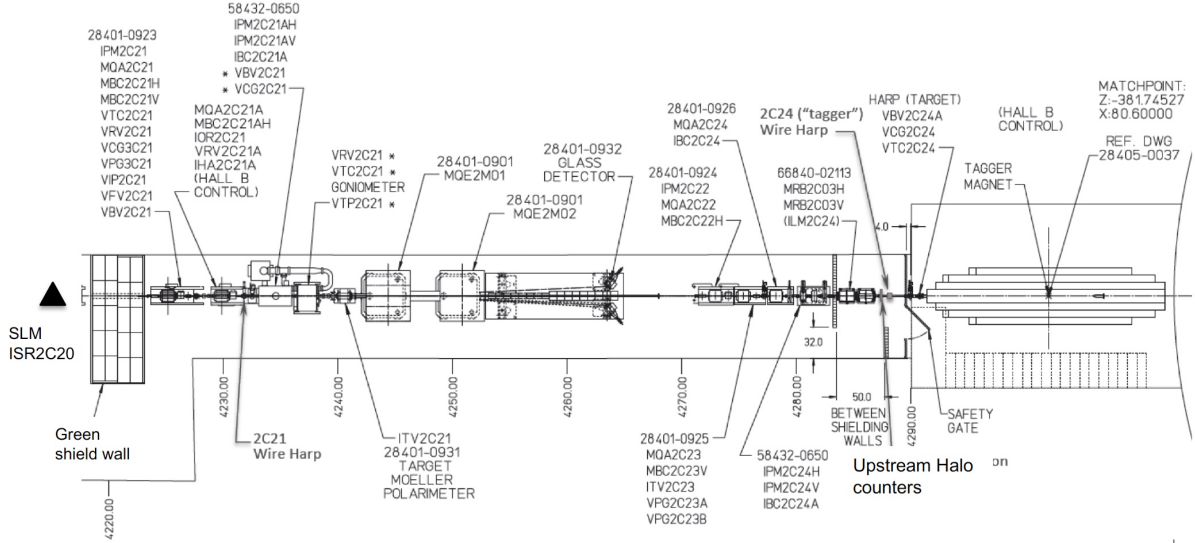


Figure 1: Overhead view of the 2C beamline in the tunnel upstream of Hall B. **Not the final figure.**

40 rameeters and to protect CLAS12 detectors against errant
 41 beam motion. As will be demonstrated, excellent qual-
 42 ity and stability of the CEBAF beams, coupled with the
 43 Hall-B beamline protection systems, allowed running
 44 the CLAS12 detector at the design luminosity.

45 2. Hall-B Beamline Design

46 As was described in Ref. [3], the Hall B beamline
 47 is divided into two segments, the so-called “2C” line
 48 from the Beam Switch Yard (BSY) following beam ex-
 49 traction from the CEBAF accelerator to the hall proper,
 50 and the “2H” line from the upstream end of the experi-
 51 mental hall to the beam dump in the downstream tunnel.
 52 The beamline upstream of CLAS12 is furnished with a
 53 number of quadrupoles, corrector dipoles, and beam di-
 54 agnostic tools, grouped into sections. Accelerator op-
 55 erators have exclusive control of these devices and use
 56 this instrumentation to tune and deliver the beam to the
 57 CLAS12 target located approximately at the geometri-
 58 cal center of the hall. In addition to the devices used
 59 by accelerator operations, there are several beam pos-
 60 ition, current, polarization, and halo monitors that are
 61 controlled and monitored by Hall-B shift personnel.

62 For high-energy operation of CLAS12, the 2C beam-
 63 line as described in Ref. [3] was modified to include
 64 the Møller polarimeter located in the upstream tunnel
 65 of the hall (see Fig. 1) and an intermediate beam dump

66 just upstream of the hall. Additionally, the 2H beam-
 67 line (Fig. 2) now includes a cryogenic target and a tung-
 68 sten shield downstream of the target inside the CLAS12
 69 torus magnet bore. The Møller polarimeter is used to
 70 periodically measure the longitudinal beam polarization
 71 and is discussed in more detail in Sec. 4. The other com-
 72 ponents are discussed immediately below.

73 2.1. Intermediate beam dump before CLAS12

74 In order to prevent radiation damage to the sensitive
 75 detectors during the initial beam tune, or when errant
 76 beam may be sent to the hall, or during the beam polar-
 77 ization measurements with the Møller polarimeter,
 78 the beam has to be terminated upstream of CLAS12.
 79 For these operations the Hall-B tagger dipole magnet is
 80 used to deflect the primary beam and secondary scat-
 81 tering products. During low-energy operations, the tag-
 82 ger dipole directs the beam into the tagger beam dump
 83 in the hall floor upstream of the CLAS12 spectrome-
 84 ter. The highest energy beam that can be directed to this
 85 dump is limited to 6.2 GeV by the maximum field of the
 86 tagger dipole, 1.76 T [4]. At higher energies, a few op-
 87 tions for the intermediate beam dump were considered
 88 during the design stage with the optimal solution being
 89 to dump the beam inside the bore of the tagger magnet
 90 yoke. The design of the intermediate dump was based
 91 on full FLUKA [5] simulations and on thermal finite-
 92 element analysis. The two main parameters that were

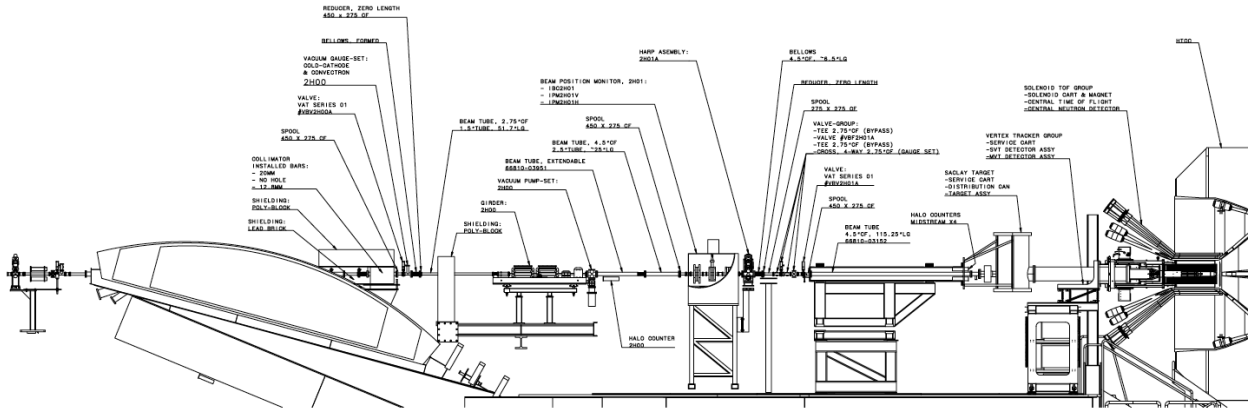


Figure 2: Beamline in the hall, upstream of the CLAS12 target. Not the final figure.

studied were the radiation levels at the location of the CLAS12 tracking detectors and the temperature rise in the magnet yoke when up to 10 nA of continuous wave (CW) electron beam is dumped on the yoke.

The FLUKA simulations were used to determine background radiation levels at the tracking detectors for different configurations of the dump and compared with radiation levels from various targets and beam currents at the design luminosity. It was found that acceptable background radiation levels from the dump occur when the beam is steered into the yoke at approximately 33 cm from the upstream entrance to the tagger magnet bore, as shown in Fig.3. This is done by setting the tagger magnetic field to be $I(A) = 43.491 \times E(\text{GeV}) - 0.076$, where I and E are the tagger power supply current and the beam energy, respectively.

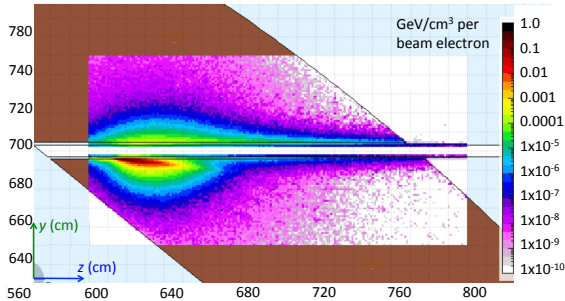


Figure 3: Distribution of energy in the yoke of the tagger dipole magnet from dumping a 10 nA, 11 GeV beam on the yoke at ~ 33 cm from the upstream entrance to the bore of tagger. Horizontal and vertical scales are distances in cm and energy deposition (in GeV/cm^3) is indicated by the color scale. The brown region indicates the cross section of the tagger yoke.

The FLUKA simulations were also used to guide the design of the shielding around and just downstream of the tagger magnet yoke. The shielding includes lead, borated polyethylene, and concrete blocks. Figure 4 shows the 1-MeV neutron equivalent fluency for the background from the dump and for various beam/target configurations as a function of the position along the beamline. In the graph, the yoke dump position is at approximately -900 cm and the CLAS12 target is at ~ 400 cm. The figure shows that at the location of the CLAS12 target, the designed shielding configuration (green points) results in radiation levels from the yoke comparable to levels for running on a carbon target at the full design luminosity.

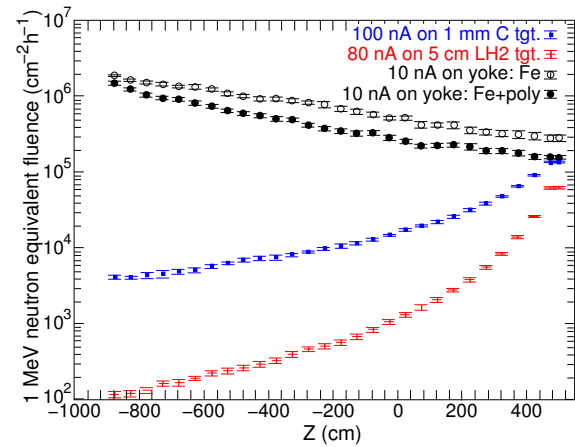


Figure 4: FLUKA simulation of radiation levels in the hall from dumping a 10 nA, 11 GeV beam on the tagger magnet yoke compared to the radiation levels from nominal running on hydrogen and carbon targets.

123 To assess the temperature increase in the yoke, a thermal
 124 finite-element analysis was set up using ANSYS
 125 Workbench v18 [6]. A simplified CAD model of the
 126 yoke was imported and modified to include a cylindrical
 127 heat load representing the beam. The heating pro-
 128 file from the deposition of 1 kW of power in a cylin-
 129 der of one Moliere radius ($r = 1.7$ cm) and 10 radi-
 130 ation lengths (17 cm) of iron was calculated. Conser-
 131 vatively, adiabatic boundary conditions were applied to
 132 the outer surfaces of the yoke. The model was solved as
 133 a transient thermal analysis with 100 time points over
 134 3600 seconds. At the dump location, the tempera-
 135 ture was found to initially increase rapidly and then sta-
 136 bilized to a maximum temperature increase of $\Delta T = 54^\circ\text{C}$
 137 as the heat dissipates throughout the yoke volume (see
 138 Fig. 5). Due to the very large volume and heat capac-
 139 ity of the yoke, the temperature is not expected to rise
 140 much higher even for longer beam application times.

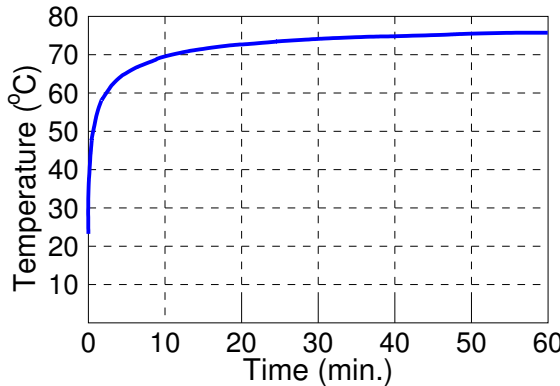


Figure 5: The heat distribution after 60 minutes of beam exposure at the dump location is shown. The highest temperature in the yoke is at the region of the impact and is 76°C assuming an initial uniform temperature of 22°C .

141 2.2. Cryogenic target

142 Hall B experiments are grouped into running periods
 143 according to beam energy and targets. So far two types
 144 of cryogenic targets have been used for experiments;
 145 liquid hydrogen (LH_2) and liquid deuterium (LD_2). The
 146 Hall-B cryotarget system from the 6 GeV era [1] has
 147 been modified for CLAS12 operation. The current tar-
 148 get cell is a 20-mm diameter, 50-mm long Kapton cylin-
 149 der with 10-mm-diameter, and 30- μm -thick aluminum
 150 entrance and exit windows. The typical target density is
 151 71 mg/cm^3 for LH_2 and 169 mg/cm^3 for LD_2 . Figure 6
 152 shows the design rendering of the target cell inside the
 153 scattering chamber. The scattering chamber is made of
 154 Rohacell XT110 foam (density $\rho = 0.110 \text{ g/cm}^3$) and is

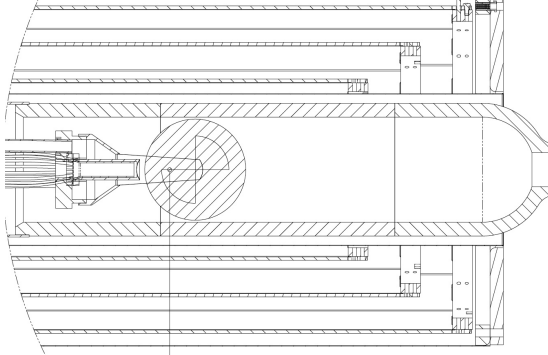


Figure 6: Sketch of the cryogenic target showing the target cell, beam offset monitor, and scattering chamber with associated plumbing and structural supports. **Not the final figures.**

155 ~45 cm long with a 100 mm outer diameter such that it
 156 fits within the CLAS12 silicon tracker (SVT) (described
 157 elsewhere in this volume) and provides a minimal ma-
 158 terial thickness for scattered particles from the target to
 159 the CLAS12 detectors.

160 A beam halo monitor is integrated within the tar-
 161 get cell. This device consists of a 40-mm-long glass
 162 cylinder with inner and outer diameters of 10 mm
 163 and 12 mm, respectively, mounted directly on the up-
 164 stream window of the target cell with its axis parallel
 165 to the beamline and with 16 optical fibers attached to
 166 the upstream perimeter of the cylinder. Light gener-
 167 ated in the cylinder from interactions of the beam halo
 168 or from back-scattered secondaries are readout with a
 169 multi-anode photomultiplier tube. The device, called
 170 the beam-offset monitor (BOM), is used to monitor the
 171 beam position at the target (see discussion below).

172 The scattering chamber extends downstream of the
 173 Central Detector. There is a 50- μm -thick aluminum
 174 window on the downstream end of the scattering cham-
 175 ber that closes the upstream vacuum beamline (from the
 176 accelerator to the CLAS12 target). The downstream
 177 vacuum beamline starts after a 60-cm-long air gap af-
 178 ter the scattering chamber and ends at the beam dump.

179 In addition to the cryogenic targets mentioned above
 180 and already used in two experiments (LH_2 and LD_2),
 181 there will be experiments that will use nuclear targets
 182 in the form of thin foils and experiments with polarized
 183 targets. The nuclear target assembly is similar to the
 184 cryogenic target cell except that various target foils will
 185 be inside the cell instead of a liquid. The cryotarget sup-
 186 ply lines will be used to flow helium gas through the cell
 187 to dissipate heat in the foils from the beam. Two types
 188 of polarized targets will be used for CLAS12 experi-
 189 ments [7]; dynamically (longitudinally) polarized am-

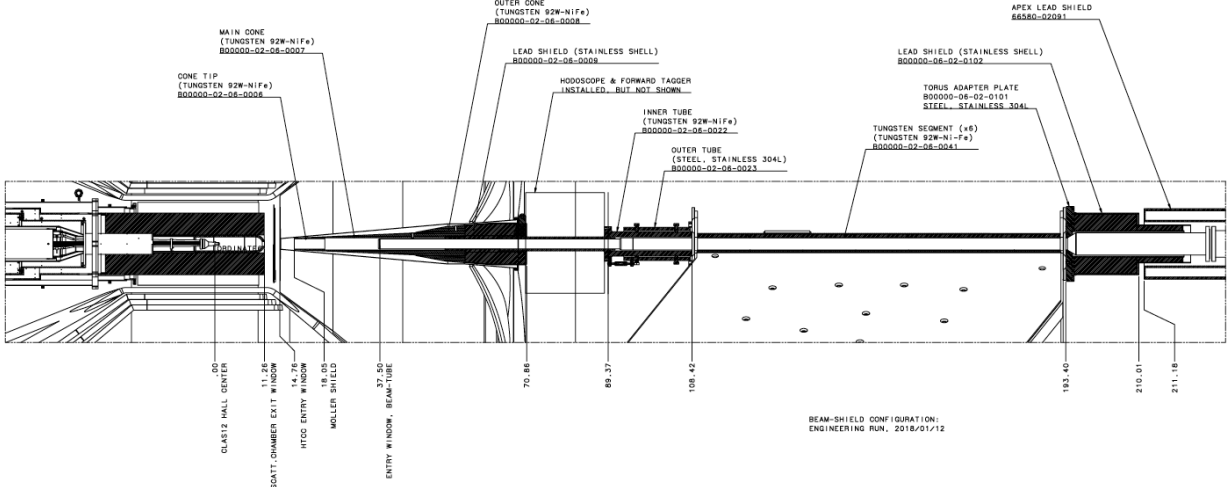


Figure 7: Tungsten shielding downstream of the target, through the torus magnet bore. **Not the final figure.**

monia (NH_3) and deuterated ammonia (ND_3), and a polarized solid HD target in a frozen spin mode.

2.3. Shielding downstream of the target

Special care was taken to protect the CLAS12 detectors from beam-induced background radiation. The main sources of the background are small-angle electron scattering along with electromagnetic processes such as bremsstrahlung, pair production, and Møller scattering. These interactions produce photons, electrons, and positrons that can flood the tracking detectors. GEANT4 simulations of CLAS12 have been used to study backgrounds and design appropriate shielding to reduce the levels of background radiation. The shielding design takes advantage of the 5-T longitudinal magnetic field around the target that is generated by the Central Detector superconducting solenoid magnet. This strong longitudinal magnetic field causes low-energy particles to spiral forward and away from the detectors and into the shielding far downstream of the target. The heavy shielding materials (lead and tungsten) contain the background and either absorb it or guide the flux of particles out the downstream end of CLAS12 without interacting in the detectors.

Because CLAS12 will run with and without the Forward Tagger (FT) (described elsewhere in this volume) in use, two shielding configurations were designed. Figure 7 shows the configuration when the FT is in use. The shielding starts with a tungsten cone with a 5-cm diameter hole at the center for the beamline. When the FT is in use, the tungsten cone is mounted directly to

the FT central support, which is also made from tungsten. In this case, the angular acceptance of particles scattered from the target starts at $\sim 2^\circ$. For the configuration without the FT, a large diameter lead cylinder is inserted between the FT central support (after removing the FT tracker) and the tungsten cone, thus moving the cone closer to the target. In this case the acceptance for forward scattered particles starts at $\sim 5^\circ$. The shielding elements also include cylindrical tungsten absorbers inside the torus bore, a tungsten shield around the FT mounting fixture to the torus, and a lead-tungsten shield downstream of the torus.

One of the main criteria for the shielding design is to maintain an occupancy rate in the drift chambers (described elsewhere in this volume) of less than 4% since higher occupancies adversely affect the track reconstruction efficiency. Drift chamber occupancies were simulated by accumulating hits in the detector elements over 250-ns time frames, which roughly corresponds to the time readout window for the drift chambers. The simulated beam was spread out over this time window to match the actual beam structure and was incident on the 5-cm-long LH_2 target such that the design luminosity of $10^{35} \text{ cm}^{-2} \text{ s}^{-1}$ was achieved in the simulation. The simulated target included the aluminum entrance and exit foils and the air gap downstream of the target. The final shielding configuration resulted in occupancies of less than about 3% for the FT-on configuration and less than about 1.5% for the FT-off configuration. Figure 8 shows the origins of background particles hitting the drift chambers for both shielding configurations. The

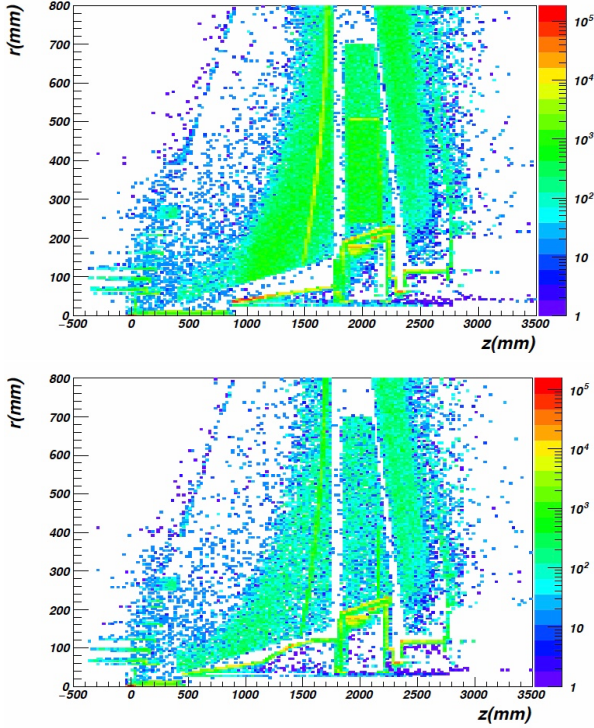


Figure 8: Tungsten shielding downstream of the target, through the torus magnet bore. This figure needs a more descriptive caption and perhaps some labels on the figure.

main source of detected events is from the target with other sources being the edges of the tungsten shields and detector enclosures. I really don't see this very clearly. I had to blow up the figure to see that the target was a source. It is clear that there is some sort of edge scattering going on but without some clarifying labels on the figure it isn't clear what these sources are. I wonder if this figure is really needed since the main point of this paragraph is that the shielding results in an acceptable occupancy has been achieved.

3. Beamline Monitoring and Performance

During a typical experiment, Hall-B shift personnel monitor key beam parameters while beam delivery is controlled by operators in the Machine Control Center. The relevant beamline elements that are used to measure and monitor the key beam parameters are listed in Table 2.

The Synchrotron Light Monitor (SLM) is a photo-multiplier tube (PMT) that measures the synchrotron light generated in the last dipole magnet that bends the beam into the Hall-B 2C beamline. The amplitude of

Table 2: Elements of the Hall-B beamline actively monitored and controlled by the experiment shift personnel.

Name and description	Distance from center of the hall (meters)
Synchrotron Light Monitor	-43.
Wire harp 2C21	-38.8
nA-BPM 2C21A	-37.6
Møller polarimeter	-31.5
nA-BPM 2C24A	-24.5
Wire harp 2C24	-22.0
Upstream halo monitors	-21.7
Hall-B tagger dipole	-17.6
Collimator	-15.3
nA-BPM 2H01	-8.0
Wire harp 2H01	-7.4
Midstream halo monitors	-3.9
CLAS12 target	0
Downstream halo monitors	7.5
Beam viewer 2H04	24.0
Dump, Faraday cup	27.0

the SLM PMT signal is proportional to the beam current and is used to measure the helicity dependence of the beam charge. Due to its dependence on the beam position, it cannot be used as a long term beam current measurement device.

The nano-amp Beam Position Monitors (nA-BPMs) [8] measure the beam current and relative beam position in the transverse, or x - y , plane (z is along the beam direction). The beam position in each direction is measured to an absolute accuracy of 50 μm . The beam current can be measured to an accuracy of $\sim 1\%$ at beam currents above 10 nA, stable over weeks of running. Information from the nA-BPMs can also be used in a feedback loop to keep the beam position fixed.

The wire harps [9] are used to measure the transverse beam profile. These are devices with 25- μm tungsten wires mounted in the horizontal and vertical directions on a support fork that moves the wires into the beam at 45°. As the harp moves into beam, count rates from beam halo counters are combined with the wire position information to determine the beam profile. Since this is an invasive measurement, it is performed primarily during the beam setup or when other devices indicate a problem with the beam.

The beam halo counters are PMT-based devices located at various positions along the beamline and are mounted very close to the beam; usually strapped directly to the beam pipe. The PMTs have either scin-

300 tillating or Cherenkov-light-producing plastic mounted 352
301 on the photocathode. In addition to providing count 353
302 rates for the wire harps, these counters are sensitive to 354
303 any beam halo or undesirable beam interactions. These 355
304 counters are the main tools to monitor beam-induced 356
305 background in the hall and along with the BOM provide 357
306 feedback signals for the machine fast shutdown system 358
307 (FSD). The FSD will stop beam delivery in the case of 359
308 excessively high background rates in order to protect the 360
309 detectors. 361

310 Other devices that Hall B uses to monitor and measure 362
311 beam parameters are the Møller polarimeter located 363
312 in the upstream tunnel for beam longitudinal polarization 364
313 measurement, a Faraday cup in the downstream tunnel 365
314 (electron beam dump) for precise beam current 366
315 measurement, and a beam viewer that looks at a 367
316 retractable fluorescent screen installed before the Faraday 368
317 cup for visual verification of beam transport to the 369
318 dump. 370

319 In Fig. 9, the main Graphical User Interface (GUI) for 371
320 monitoring the beam delivery and beamline devices is 372
321 shown. The underlying software is EPICS [10] for the 373
322 real-time control and monitoring of devices. The user 374
323 interface is built using the CS-Studio tools [11]. All 375
324 variables available in EPICS are archived using the Jefferson 376
325 Lab MYA data archiver [12]. 377

326 Each section of the main GUI represents a collection 378
327 of monitored quantities. In the top row, the rates of 379
328 beam halo counters and the integrated rates of CLAS12 380
329 detectors are displayed. The other information shown 381
330 at the top of the GUI are the status of the hall on the 382
331 right, the state of the beam orbit locks on the left, and 383
332 the FSD configuration in the middle. In the middle of 384
333 the GUI, beam position and current monitors are 385
334 displayed together with the target status and BOM counts. 386
335 The status and positions of moving devices such as wire 387
336 harps, collimators, and the beam blocker are displayed 388
337 in the lower middle part of the GUI. At the bottom of 389
338 the GUI the vacuum gauges, and currents and fields of 390
339 the beamline magnets and the CLAS12 superconducting 391
340 magnets are shown. The digital output of the beam 392
341 viewer camera is displayed in the lower right corner. 393
342 There is also information on beam parameters and beam 394
343 helicity in the upper left quadrant of the GUI. For convenience 395
344 of monitoring, a timeline of counter rates, along 396
345 with BPM positions and beam current readings can be 397
346 displayed separately. 398

347 Establishing a production quality electron beam for 399
348 experiments in Hall B is a two-step process. First, the 400
349 beam is delivered and tuned in the 2C beamline in the 401
350 Hall-B upstream tunnel. During this tuning process the 402
351 beam is dumped on the tagger yoke to protect CLAS12 403

detectors from excessive radiation exposure. Once the 2C beamline is tuned, the beam is then sent to the downstream electron dump and tuned onto the CLAS12 target. During the tuning process, the beam profile and transverse position are optimized using the information from the wire harps, the nA-BPMs, and the beam halo counters. The beam is accepted for physics production running when all the relevant parameters are within expected limits. After production beam has been established, limits on the halo counter rates, beam positions, and beam current are set in the CS-Studio alarm system to help Hall-B shift personnel to monitor the beam quality when running experiments.

3.1. Beam profile and position stability

Establishing and maintaining a high-quality beam is important for obtaining high-quality physics data. Once the beam has been established, scans using the wire harps and nA-BPMs are stored in the MYA archive and are used as reference values over the course of an experimental running period. Figure 10 shows the x - and y -profiles measured with wire harps 2C21 and 2H01, located in the upstream tunnel of Hall B and at 7.4 m upstream of the target, respectively. During these measurements, the beam was delivered to the Faraday cup. Figure 11 shows a histogram of the x - and y -widths for sixteen 2H01 harp scans taken over a two month running period. The beam width in both directions fluctuates between $180 \mu\text{m}$ to $300 \mu\text{m}$ with an average value of $250 \mu\text{m}$.

After the beam has been established for physics running, its position and current stability are continuously monitored using the halo counter rates and the nA-BPMs. Figure 12 shows the distribution of the x - and y -positions about the mean at the 2H01 nA-BPM. The RMS of both distributions is on order of $20 \mu\text{m}$. Such stability is largely due to use of the beam orbit lock system that uses the position readings of nA-BPMs to drive horizontal and vertical correctors that keep the position of the beam at the set points established at the start of a running period.

3.2. Beam charge measurement

An accurate measurement of the total amount of beam charge incident on the target during an experiment is vital for the measurement of experimental cross sections. The Hall-B Faraday cup (FC) is the main tool to obtain an accurate *absolute* beam current measurement. A description of the Faraday cup and its readout electronics can be found in Ref. [1]. Since the Faraday cup does not have active cooling, it is limited to 175 W

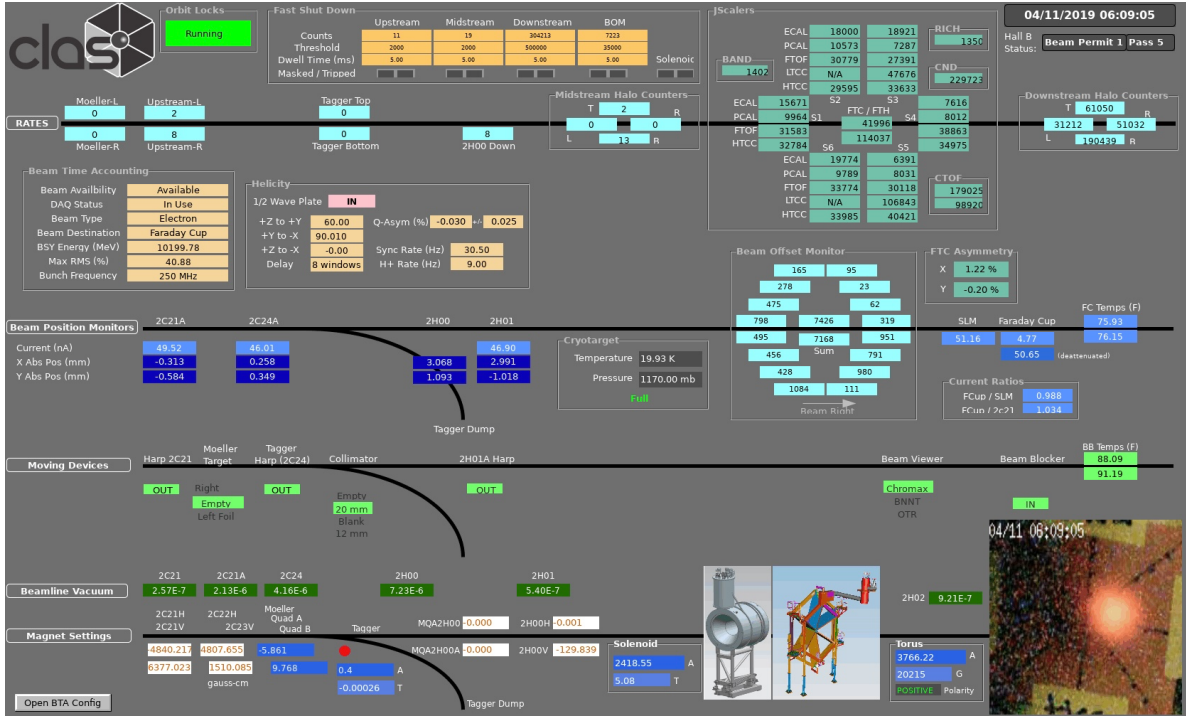


Figure 9: The main Graphical User Interface (GUI) for monitoring of beamline devices, detector rates, and magnets.

of beam power for long exposures. However, most of the CLAS12 experiments will run with beam currents that exceed the power limit of the FC, thus requiring another method of measuring the beam current. The other devices used to monitor the beam current during the experiment are the nA-BPMs and the SLM, but these devices do not have the long-term stability to provide the accuracy needed over the weeks-long course of an experiment.¹

Instead, a 5-kW beam dump can be inserted in front of the FC during high-power running. This insertable dump, or beam blocker, is a water-cooled, 28-cm-long copper cylinder (19.5 radiation lengths). While most of the beam is deposited in this beam blocker, the FC still measures a leak-through charge that is proportional to the total beam current with a very high accuracy of better than 0.5%. In order to use the FC current measurement with the blocker in, a beam-current attenuation factor, A , must be determined for every beam energy, so that the beam current is given by $I = AI_{FC}^{in}$, where I_{FC}^{in} is the beam current measured at the FC when the beam blocker is in.

To calibrate the attenuation factor, first, a scan of the beam current up to the highest current required by the experiment is done without the beam blocker. The scan is quick so as to not overheat the FC. These data are used to calibrate the nA-BPM current readings relative to the FC with a calibration factor given by $C = I_{BPM}/I_{FC}$, where I_{BPM} and I_{FC} are the currents measured by the nA-BPM and FC, respectively. The left panel of Fig. 13 shows a distribution of C for a range of beam currents from 15 to 80 nA at a beam energy of 10.67 GeV using the 2C21 nA-BPM. The distribution has a mean of $\langle C \rangle = 1.057$ and Gaussian width of $\sigma_C = 0.0038$, which we use to determine the relative uncertainty in the calibration factor of $\delta C/C = \sigma_C/\langle C \rangle = 0.36\%$.

In the second step, a similar current scan is performed but with the insertable beam blocker in place. Using the now calibrated values of the nA-BPM current reading from the first step, the attenuation factor is given by $A = I_{BPM}^{in}/I_{FC}^{in}$. The distribution of A is shown in the right panel of Fig. 13, which has also been obtained for a range of beam currents from 15 to 80 nA at a beam energy of 10.67 GeV using the 2C21 nA-BPM. The distribution has a mean of $\langle A \rangle = 9.807$ and a Gaussian width of $\sigma_A = 0.0306$, which leads to a relative uncertainty of $\delta A/A = \sigma_A/\langle A \rangle = 0.31\%$. Combining the uncertain-

¹The calibration of the nA-BPMs relative to the FC remains stable within a few % for a period of time sufficient for coarse monitoring of the beam current during the experiment.

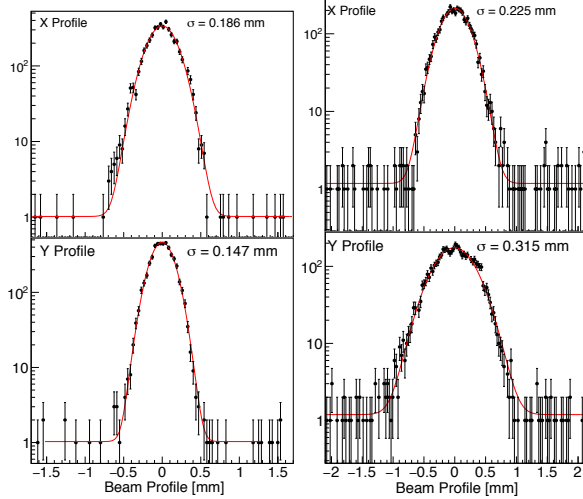


Figure 10: Beam x - (top) and y -profiles (bottom) measured using the wire harp scanners at 2C21 (left) and at 2H01 (right). The red curve is a Gaussian fit with the width shown by the σ values.

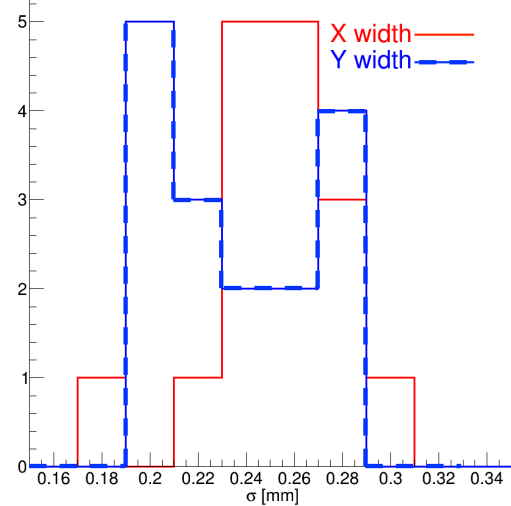


Figure 11: Beam width measured with the 2H01 wire harp over two months of running. The x -width is shown in solid red and the y -width is shown in dashed blue.

ties from the calibration of the nA-BPMs and the attenuation factor leads to a total relative uncertainty in the blocker-in FC current measurement of $\delta I_{FC}/I = 0.48\%$.

A simultaneous measurement of the attenuation factor has been done using the 2C24 nA-BPM resulting in $\langle A \rangle = 9.809$, which agrees well with the 2C21 nA-BPM measurement. More details of this calibration can be found in Ref. [13]. Results obtained for other energies are shown in Table 3 with details found in Ref. [14].

Beam energy (GeV)	FC Attenuation
6.4	16.28
6.6	16.24
7.54	14.90
10.2	9.96
10.67	9.81

Table 3: FC attenuation factors for different beam energies. The estimated relative uncertainty of the attenuation factor is $< 0.5\%$.

4. Møller Polarimeter

Determination of the electron beam polarization is done in Hall B using a coincidence Møller polarimeter. The polarimeter is based on $e + \bar{e} \rightarrow e + e$ elastic scattering (Møller scattering). A detailed description of Møller scattering is presented in Ref. [15].

For a longitudinally polarized electron beam incident on a longitudinally polarized electron target, the center-

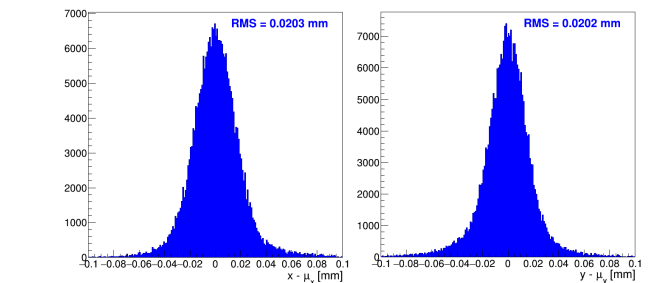


Figure 12: Beam position deviations, $x - \mu_x$ (left) and $y - \mu_y$ (right), over a month of running as measured by the 2H01 nA-BPM.

of-momentum (CM) frame cross section is given by [16, 17]

$$\frac{d\sigma}{d\Omega} = \frac{d\sigma_0}{d\Omega} (1 + P_B A_{zz} P_T), \quad (1)$$

where $d\sigma_0/d\Omega$ is the unpolarized cross section, P_B and P_T are the longitudinal components of the beam and target polarization, respectively, and A_{zz} is the analyzing power. The unpolarized cross section and analyzing power can be precisely calculated through QED, which gives

$$\frac{d\sigma_0}{d\Omega} = \left(\frac{\alpha (3 + \cos^2 \theta_{CM})}{2m_e \gamma \sin^2 \theta_{cm}} \right)^2, \quad (2)$$

and

$$A_{zz} = -\frac{(7 + \cos \theta_{CM}) \sin^2 \theta_{CM}}{(3 + \cos^2 \theta_{CM})^2}, \quad (3)$$

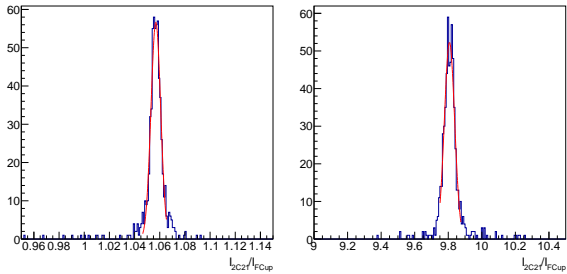


Figure 13: The ratio of beam currents measured by the 2C21 nA-BPM and the Faraday cup without (left) and with (right) the insertable beam blocker. Each distribution has been fit with a Gaussian to obtain the means and widths given in the text.

both operated in a dispersive mode to separate the scattered electrons for the unscattered beam electrons, a pair of detectors, and lead shielding between the second quadrupole and the detectors to reduce background. The detectors consist of scintillating fibers packed with lead powder to form a 15.6-cm wide, 9.0-cm high, and 25-cm deep block with a light guide and read out with a PMT. The detectors are surrounded by lead bricks with a scattered-particle aperture of 7.62 cm in the horizontal direction and 5.0 cm in the vertical direction. The locations of the quadrupoles and detectors along with the quadrupole fields were determined by simulations of the layout. The locations and fields were adjusted in the simulation so that $\theta_{CM} = 90^\circ \pm (4^\circ - 4.5^\circ)$.

where α is the fine structure constant, θ_{CM} is the center of momentum scattering angle, m_e is the electron mass, and $\gamma = \sqrt{(E + m_e)/2m_e}$ with E the lab energy of the incident electron. From the above formulas, one sees that A_{zz} has a maximum magnitude of 7/9 at $\theta_{CM} = 90^\circ$, which is the central scattering angle for our polarimeter.

Forming the beam-helicity-dependent asymmetry gives

$$A = \frac{\frac{d\sigma}{d\Omega_+} - \frac{d\sigma}{d\Omega_-}}{\frac{d\sigma}{d\Omega_+} + \frac{d\sigma}{d\Omega_-}} = A_{zz}(\theta_{CM}) P_B^z P_T^z, \quad (4)$$

where the \pm refers to cases where the beam helicity and the target polarization are aligned or anti-aligned. The asymmetry can be measured from the yields according to

$$A = \frac{N_+ - N_-}{N_+ + N_-} = \langle A_{zz} \rangle P_B^z P_T^z, \quad (5)$$

where $\langle A_{zz} \rangle$ is the effective analyzing power corrected for the finite-angle acceptance of the polarimeter and atomic-electron motion (also known as the Levchuk effect [18]).

The CLAS12 Møller polarimeter detects the scattered electrons in coincidence near $\theta_{CM} = 90^\circ$, the peak of A_{zz} . The coincidence method has the advantage, as compared to single-arm Møller polarimetry, of producing a clean data set without having to do energy-dependent background subtractions (see, for example Ref. [19]). Accidental background rates are typically less than 10% of the real coincident rate for our polarimeter. The accidental rate is measured and included as a correction.

4.1. Polarimeter Design

The layout for the polarimeter is shown in Fig. 14. The essential elements of the polarimeter include a polarized target system, a pair of quadrupole magnets

4.1.1. Polarimeter Target

The target system has a pair of 25-μm-thick permendur foils on a remotely controlled insertion table housed in a vacuum chamber, as shown in Fig. 15. Permendur is an iron-cobalt alloy (49% Fe, 49% Co, 2% Va) that has a saturated polarization of approximately 8% along the plane of the foil when subjected to a magnetic field of greater than about 40 G. To create a longitudinally polarized target, the plane of a foil is oriented at $\pm 20^\circ$ relative to the beamline and subjected to a longitudinal magnetic holding field produced by a pair of Helmholtz coils on either side of the target chamber. Since only the longitudinal component of the polarization contributes to the measured asymmetry, the target polarization used in Eq. 5 is $P_T^z = P_T \cos 20^\circ$.

The polarization of the permendur target is related to the magnetization, M , of the foil by [20]

$$P_T = M(4.546 \times 10^{-5} \pm 2.9 \times 10^{-7}), \quad (6)$$

where M is measured in units of G. The foil magnetization is measured in a separate setup consisting of a solenoid coil used to produce the magnetizing field, H , into which the target foil is placed and a pickup coil that is located at the center of the foil. A fixed current is applied to the solenoid to polarize the target. The direction of the current is then flipped over a time period of 0.15 s leading to an induced voltage across the pickup coil. A typical pickup-coil signal is shown in Fig. 16, which was measured with a digital storage oscilloscope. The flat part of this signal (highlighted by the black constant fit) corresponds to the changing applied field while the narrow peak in the middle of the signal results from the change in the target foil magnetization. Applying Faraday's law to the flat part of the signal (using the fit to interpolate under the peak) yields

$$\int_H V dt = 2HN_T \langle A_{coil} \rangle \rightarrow H = \frac{\int_H V dt}{2N_T \langle A_{coil} \rangle}, \quad (7)$$

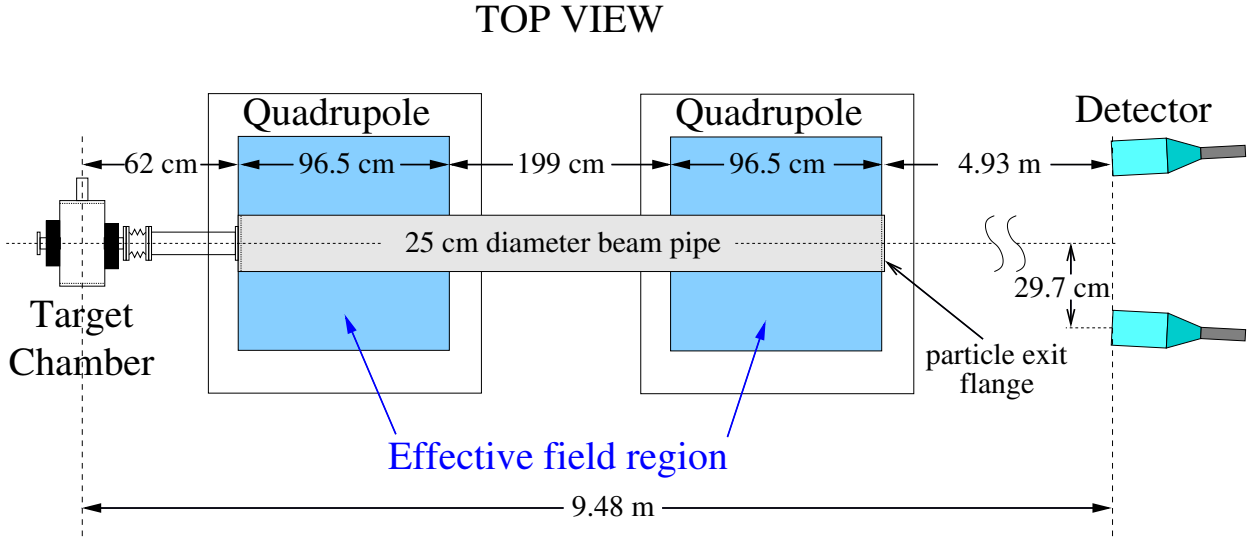


Figure 14: Layout of the CLAS12 Møller polarimeter. Detector shielding is not shown.

557 where $\int_H V dt$ is the area under the pickup coil signal
 558 excluding the peak, N_T is the number of turns in the
 559 pickup coil, and $\langle A_{\text{coil}} \rangle$ is the average cross-sectional
 560 area of the pickup coil. Since the magnetization is
 561 related to the total field, B , and the applied field, H ,
 562 through $4\pi M = B - H$, then

$$563 M = B - H = \frac{1}{4\pi} H \left(\frac{\int_{\text{total}} V dt - \int_H V dt}{\int_H V dt} \right), \quad (8)$$

564 where $\int_{\text{total}} V dt$ is the total area of the signal. Fig-
 565 ure 17 shows a typical saturation curve for the target,
 566 i.e. how the target polarization depends on the ap-
 567 plied field. Measurements were done with two differ-
 568 ent pickup coils with the difference between the two
 569 results indicating the systematic uncertainty associated
 570 with knowledge of the coil geometry. For this foil, the
 571 polarization saturates at a value of $7.31 \pm 0.08\%$, where
 572 the uncertainty is a combination of the statistical uncer-
 573 tainties from the linear fits of the saturation region of
 574 the curves and the variation between the two measure-
 575 ments. Additional uncertainties associated with con-
 576 verting from M to P_T (Eq. 6), the uncertainty from esti-
 577 mated variations in the target material thickness, and the
 578 uncertainty in the target angle relative to the beam lead
 579 lead to an overall uncertainty of 0.13% and a total relative
 580 uncertainty $\delta P_T^z / P_T^z = 0.018$.

581 4.2. Analyzing Power Corrections and Uncertainties

582 Simulations have been performed to estimate effects
 583 due to atomic motion of the electrons and to estimate

584 uncertainties associated with the polarimeter geometry.
 585 The simulation begins by randomly selecting scattering
 586 angles θ_{CM} and ϕ_{CM} and then transports the scattered
 587 electrons through the magnets and towards the detec-
 588 tors. For events in which both electrons hit the detec-
 589 tors we determine an average analyzing power, $\langle A_{zz} \rangle$.
 590 The motion of the atomic electrons has been included in
 591 the simulation according to Ref. [18]. Figure 18 shows
 592 $\langle A_{zz} \rangle$ as a function of beam energy both with (orange)
 593 and without (blue) atomic-electron motion included in
 594 the simulation. The green curve is a fit to the points
 595 $\langle A_{zz} \rangle = -0.777123 + (2.9249 \times 10^{-3})/E$. The estimated
 596 relative uncertainty is $< 0.01\%$ and was determined by
 597 looking at variations in $\langle A_{zz} \rangle$ for reasonable variations in
 598 the geometry (locations of quadrupoles and detectors)
 599 and magnetic fields.

600 4.3. Beam polarization measurements

601 Beam polarization measurements are usually done
 602 on a weekly basis or after changes to the accelera-
 603 tor configuration. The shift personnel use what is in
 604 essence a push-button GUI interface shown in Fig. 19.
 605 The user selects which target to use (left or right)
 606 and the Helmholtz coil polarity. The settings for the
 607 quadrupoles are automatically calculated based upon
 608 the beam energy. Individual Møller runs are usually
 609 done for both targets with a statistical precision of
 610 $\pm 1.5\%$, which is slightly smaller than the total sys-
 611 tematic uncertainty. The underlying software calculates the
 612 beam polarization using the beam-helicity-gated true

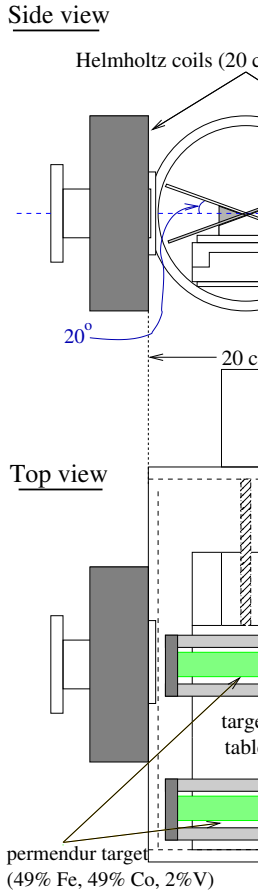


Figure 15: Layout of the CLAS12 Møller polarimeter target chamber. Shown with the beam-left target inserted.

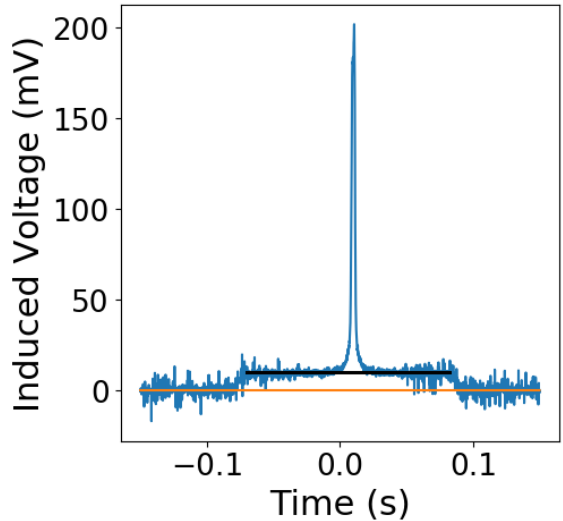


Figure 16: Target pickup coil signal showing induced voltage as a function of time. The flat part of the signal (fit with black line) corresponds to the changing applied Helmholtz field, H , while the sharp peak near the middle corresponds to the flip in the target magnetization.

and accidental coincidence rates from the Møller detectors along with the beam-helicity related charge asymmetry measured using the SLM. At the end of a Møller run the beam polarization is stored in the database and displayed in the GUI, as seen in the upper right quadrant of Fig. 19.

Results of beam polarization measurements taken during the fall 2018 run period are shown in Fig. 20. There are two distinct regions of beam polarization with average polarizations of $85.95\% \pm 1.29\%$ and $89.22\% \pm 2.51\%$. These two regions differ by settings of the angle, θ_W of the Wien filter in the injector. The initial setting of the Wien-filter angle was set to maximize the beam polarization in Hall B and is based on a calculation of the electron spin precession in the accelerator. However, the polarization in the early part of the running period fell below the expected maximum of about 90%, which was measured at the injector by a Mott polarimeter, indicating an incorrectly calculated θ_W . In order to find the optimum value of θ_W , two more Møller measurements of the beam polarization in Hall-B were performed at $\theta_W = 25^\circ$ and 70° . The result of these measurements along with the average at 40° are shown in Fig. 21. Fitting these three points with a function of $a \cos(\theta_W - b)$ (dashed curve), where a and b are fit parameters, shows that the maximum polarization of about 90% in Hall B occurs for $\theta_W \approx 40^\circ$.

Figure 20 has two sets of Hall-B polarimeter mea-

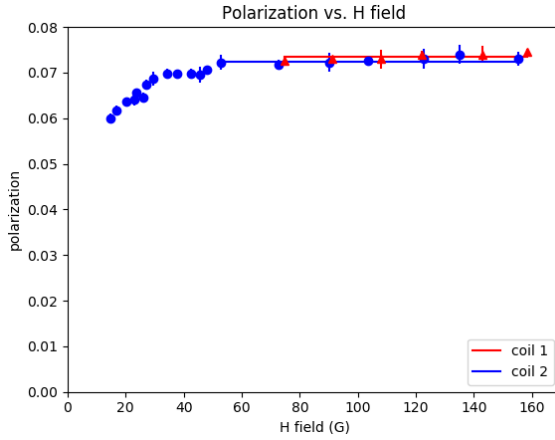


Figure 17: Target polarization vs. applied magnetic field, H , measured with two different pickup coils. A constant fit to the flat part of the curves yields values of $7.35 \pm 0.04\%$ for coil 1 (red diamonds) and $7.24 \pm 0.05\%$ for coil 2 (blue dots).

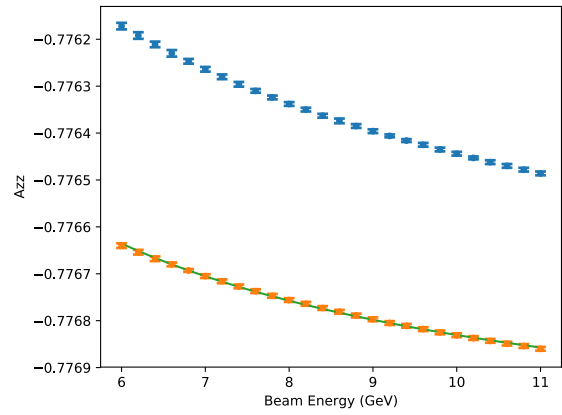


Figure 18: Average analyzing power $\langle A_{zz} \rangle$ as a function of beam energy from simulation. The orange/blue points include/exclude motion of the atomic electrons. The error bars are statistical only. The green curve on the orange points is a fit given in the text.

641 sUREMENTS done with and without a half-wave plate. The
 642 half-wave plate rotates the electron spin by 180° . The
 643 measurements with and without the the half-wave plate
 644 agree within statistical uncertainties.

645 5. Summary

646 The first CLAS12 experiment took data successfully
 647 at three beam energies; 10.6 GeV, 6.4 GeV and 2.3 GeV
 648 with a liquid-hydrogen target. High quality beam was
 649 delivered with the beam size of $< 200 \mu\text{m}$ and the beam
 650 halo as small as 10^{-4} . The beam position was main-
 651 tained within $\sim 200 \mu\text{m}$ throughout the run by the beam
 652 feedback system and the fast shut down system worked
 653 in protecting the CLAS12 detectors sensors from errant
 654 beam exposure. With typical Møller polarimeter runs,
 655 the beam polarization can be measured to an absolute
 656 precision of $\sim 2.5\%$.

657 6. Acknowledgements

658 The authors are grateful for the outstanding efforts
 659 by the staff of the Accelerator Division and the Hall B
 660 Engineering Group at Jefferson Lab during the instal-
 661 lation and running of the experiment. We also thank
 662 the CLAS12 collaboration for manning shifts and tak-
 663 ing high quality data. This material is based upon work
 664 supported by the U.S. Department of Energy, Office of
 665 Science, Office of Nuclear Physics under contract DE-
 666 AC05-06OR23177.

- 667 [1] B. A. Mecking, et al., The CEBAF Large Acceptance Spec-
 668 trometer (CLAS), Nucl. Instrum. Meth. A503 (2003) 513–553.
 669 doi:10.1016/S0168-9002(03)01001-5.
- 670 [2] HPS update to PAC39, https://www.jlab.org/exp_prog/proposals/12/C12-11-006.pdf.
- 671 [3] N. Baltzell, et al., The Heavy Photon Search beamline and its
 672 performance, Nucl. Instrum. Meth. A859 (2017) 69–75. [arXiv:1612.07821](https://arxiv.org/abs/1612.07821), doi:10.1016/j.nima.2017.03.061.
- 672 [4] D. I. Sober, et al., The bremsstrahlung tagged photon beam in
 673 Hall B at JLab, Nucl. Instrum. Meth. A440 (2000) 263–284.
 674 doi:10.1016/S0168-9002(99)00784-6.
- 674 [5] T. T. Bhlen, F. Cerutti, M. P. W. Chin, A. Fass, A. Ferrari, P. G.
 675 Ortega, A. Mairani, P. R. Sala, G. Smirnov, V. Vlachoudis, The
 676 FLUKA Code: Developments and Challenges for High Energy
 677 and Medical Applications, Nucl. Data Sheets 120 (2014) 211–
 678 214. doi:10.1016/j.nds.2014.07.049.
- 678 [6] <https://www.ansys.com/-/media/Ansystech/corporate/resourcecenter/brochure/ansyscapabilities180.pdf>.
- 679 [7] C. Keith, Polarized Solid Targets at Jefferson Lab, PoS
 680 PSTP2015 (2015) 013. doi:10.22323/1.243.0013.
- 680 [8] R. Ursic, M. Piller, R. Flood, E. Strong, L. Turlington, 1 nA
 681 Beam Position Monitoring System, Conf. Proc. C970512 (1997)
 682 2131.
- 682 [9] M. McCaughan, M. Tiefenback, D. Turner, Improvements to
 683 Existing Jefferson Lab Wire Scanners, in: Proceedings, 4th
 684 International Particle Accelerator Conference (IPAC 2013):
 685 Shanghai, China, May 12–17, 2013, 2013, p. MOPWA076.
 686 URL <http://JACoW.org/IPAC2013/papers/mopwa076.pdf>
- 686 [10] <https://epics-controls.org>.
- 687 [11] <http://controlsystemstudio.org>.
- 688 [12] C. Slominski, https://wiki.jlab.org/lerf/images/7/75/Archive_user.pdf.
- 689 [13] R. Paremuzyan, S. Stepanyan, CLAS12 Note 2018-003 (2018).
 690 [link].
 691 URL <https://misportal.jlab.org/mis/physics/clas12/viewFile.cfm/2018-004.pdf?documentId=58>
- 691 [14] R. Paremuzyan, S. Stepanyan, CLAS12 Note 2018-004 (2018).
 692 [link].
 693 URL [https://misportal.jlab.org/mis/physics/clas12/viewFile.cfm/2018-003.7gev.pdf?](https://misportal.jlab.org/mis/physics/clas12/viewFile.cfm/2018-003.7gev.pdf)



Figure 19: Graphical user interface for Møller polarimeter operation.

documentId=57

- [15] B. Wagner, H. G. Andresen, K. H. Steffens, W. Hartmann, W. Heil, E. Reichert, A Moller polarimeter for CW and pulsed intermediate-energy electron beams, Nucl. Instrum. Meth. A294 (1990) 541–548. doi:10.1016/0168-9002(90)90296-I.
- [16] C. Møller, Ann. Phys. 14 (1932) 531.
- [17] A. A. Kresnin, L. N. Rosentsveig, J. Exp. Theor. Phys. (USSR) 32 (1957) 353.
- [18] L. G. Levchuk, The Intraatomic motion of bound electrons as a possible source of a systematic error in electron beam polarization measurements by means of a Moller polarimeter, Nucl. Instrum. Meth. A345 (1994) 496–499. doi:10.1016/0168-9002(94)90505-3.
- [19] J. Arrington, E. J. Beise, B. W. Filippone, T. G. O'Neill, W. R. Dodge, G. W. Dodson, K. A. Dow, J. D. Zumbro, A Variable energy Moller polarimeter at the MIT-Bates Linear Accelerator Center, Nucl. Instrum. Meth. A311 (1992) 39–48. doi:10.1016/0168-9002(92)90849-Y.
- [20] H. R. Band, G. Mitchell, R. Prepost, T. Wright, A Moller polarimeter for high-energy electron beams, Nucl. Instrum. Meth. A400 (1997) 24–33. doi:10.1016/S0168-9002(97)00984-4.

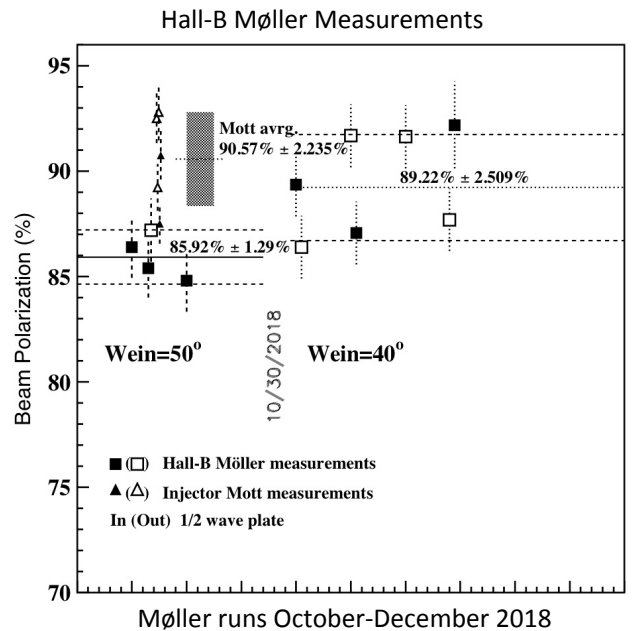


Figure 20: Beam polarization measured in Hall B during the fall 2018 running period. Prior to October 30 the measurements from the Hall-B polarimeter (squares) averaged to $85.9\% \pm 1.2\%$ (stat.), which is lower than the expected 90% from the injector Mott measurements (triangles). After the optimizing the Wien-filter angle the average polarization measured in Hall B was measured to be $89.2\% \pm 2.5\%$ (stat.). Filled and open symbols correspond to measurements made with and without a half-wave plate. Error bars are statistical only.

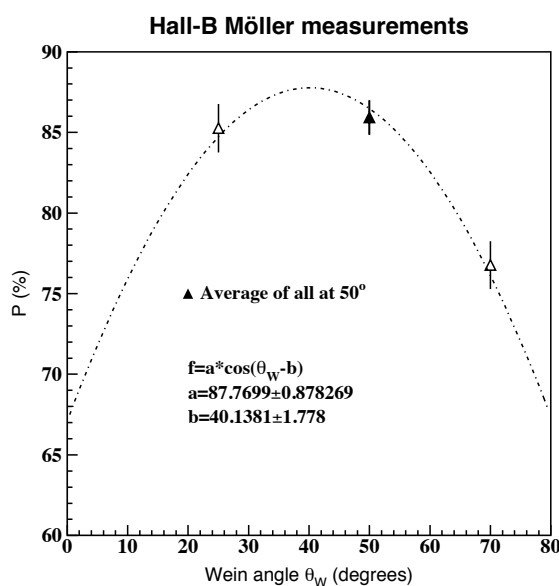


Figure 21: Beam polarization measurements at three different Wien angle settings taken during the fall 2018 run period. The dashed curve is the cosine-function fit to the data points. The filled point is the average over all measurements with the angle set to 50° and the open points are from single measurements. Error bars are statistical only.